Article |

Precision spectroscopy and laser-cooling scheme of a radium-containing molecule

S. M. Udrescu [iD][1][✉], S. G. Wilkins [iD][1][✉], A. A. Breier [iD][2],
M. Athanasakis-Kaklamanakis[3,4], R. F. Garcia Ruiz [iD][1][✉], M. Au [iD][5,6], I. Belošević[7],
R. Berger [iD][8], M. L. Bissell[9], C. L. Binnersley[9], A. J. Brinson[1], K. Chrysalidis [iD][5],
T. E. Cocolios [iD][4], R. P. de Groote[4], A. Dorne[4], K. T. Flanagan[9,10], S. Franchoo[11],
K. Gaul[8], S. Geldhof [iD][4], T. F. Giesen [iD][2], D. Hanstorp [iD][12], R. Heinke [iD][5],
Á. Koszorús[3], S. Kujanpää [iD][13], L. Lalanne [iD][4], G. Neyens [iD][4], M. Nichols[12],
H. A. Perrett [iD][9], J. R. Reilly[9], S. Rothe [iD][5], B. van den Borne [iD][4], A. R. Vernon[9],
Q. Wang [iD][14], J. Wessolek[9], X. F. Yang [iD][15] & C. Zülch[8]

Molecules containing heavy radioactive nuclei are predicted to be extremely sensitive to violations of the fundamental symmetries of nature. The nuclear octupole deformation of certain radium isotopes massively boosts the sensitivity of radium monofluoride molecules to symmetry-violating nuclear properties. Moreover, these molecules are predicted to be laser coolable. Here we report measurements of the rovibronic structure of radium monofluoride molecules, which allow the determination of their laser cooling scheme. We demonstrate an improvement in resolution of more than two orders of magnitude compared to the state of the art. Our developments allowed measurements of minuscule amounts of hot molecules, with only a few hundred per second produced in a particular rotational state. The combined precision and sensitivity achieved in this work offer opportunities for studies of radioactive molecules of interest in fundamental physics, chemistry and astrophysics.

The Standard Model of particle physics has been spectacularly successful at explaining the fundamental interactions of the known elementary particles of the universe up to TeV-scale energies. However, the Standard Model is not a complete theory of nature, as it cannot account for observations related to dark matter, dark energy, the matter–antimatter asymmetry of the universe or the spectrum of elementary particle masses[1]. Numerous Standard Model extensions have been proposed to explain these observations, often predicting stronger violations of fundamental symmetries, such as parity or time reversal, or the existence of new forces and particles[1]. A great deal of attention is therefore now focused on constraining these effects in precision experiments conducted across different energy scales.

In the last few years, precision molecular studies have emerged as a compelling platform upon which to perform these investigations[2–9]. Symmetry-violating properties of fundamental particles can add minuscule but measurable perturbations to the energies of molecular states.

[1]Massachusetts Institute of Technology, Cambridge, MA, USA. [2]Laboratory for Astrophysics, Institute of Physics, University of Kassel, Kassel, Germany. [3]Experimental Physics Department, CERN, Geneva 23, Switzerland. [4]KU Leuven, Instituut voor Kern - en Stralingsfysica, Leuven, Belgium. [5]Systems Department, CERN, Geneva 23, Switzerland. [6]Department Chemie, Johannes Gutenberg-Universitat Mainz, Mainz, Germany. [7]TRIUMF, Vancouver, British Columbia, Canada. [8]Fachbereich Chemie, Philipps-Universität Marburg, Marburg, Germany. [9]School of Physics and Astronomy, The University of Manchester, Manchester, UK. [10]Photon Science Institute, The University of Manchester, Manchester, UK. [11]Laboratoire Irène Joliot-Curie, Orsay, France. [12]Department of Physics, University of Gothenburg, Gothenburg, Sweden. [13]Department of Physics, Accelerator laboratory, University of Jyväskylä, Jyväskylä, Finland. [14]School of Nuclear Science and Technology, Lanzhou University, Lanzhou, P. R. China. [15]School of Physics and State Key Laboratory of Nuclear Physics and Technology, Peking University, Beijing, China. ✉e-mail: sudrescu@mit.edu; wilkinss@mit.edu; rgarciar@mit.edu
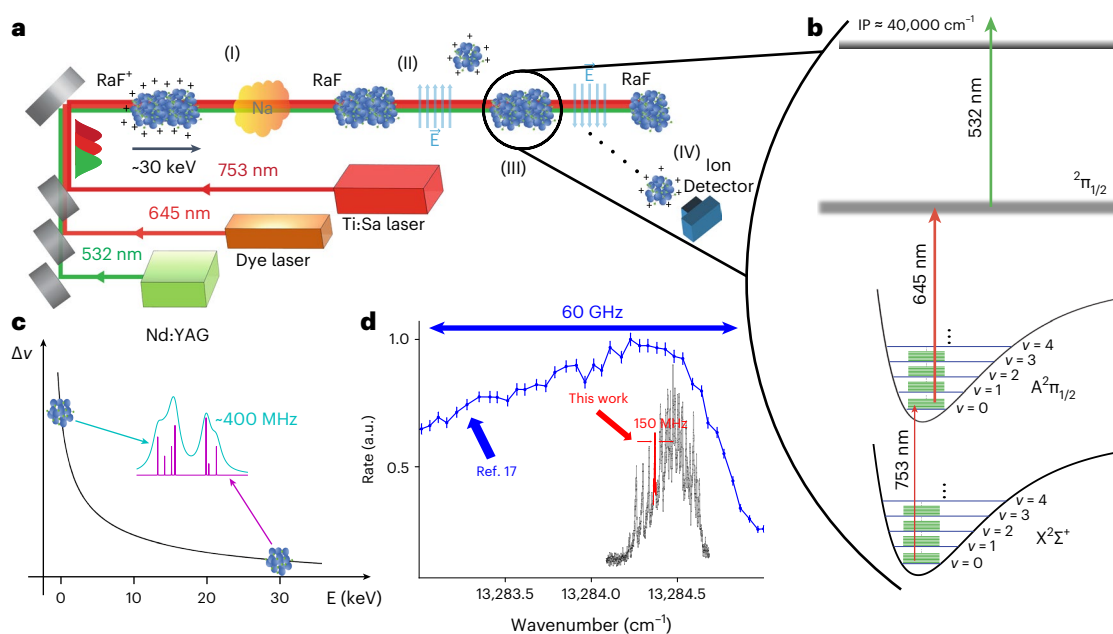
Fig. 1 | Illustration of the experimental setup. a, Mass-selected RaF$^+$ ions accelerated to ~30 keV are partially neutralized in a Na vapour (I). Residual ions are removed using a static electric field (II), and neutral molecules are overlapped collinearly with three pulsed laser beams (III). The three lasers used are shown as coloured cuboids. Their approximate wavelengths and relative timings (coloured Gaussian shapes) are indicated. Resonantly ionized molecules are deflected and detected on an ion detector (IV). **b**, Three-step ionization scheme for the RaF molecules. The first Ti:Sa laser excites the molecules from the ground X$^2\Sigma^+$ to the excited A$^2\Pi_{1/2}$ electronic state. Potential curves of the two states, vibrational (blue) and rotational (green) energy levels are shown, not to scale (v labels the vibrational quantum numbers). A second dye laser further excites the molecules to a higher-lying $^2\Pi_{1/2}$ electronic state. Finally, a neodymium-doped yttrium-aluminium-garnet (Nd:YAG) pulsed laser ionizes the molecules. The value of the ionization potential (IP) as well as the wavelengths of the lasers used are shown. **c**, At zero centre-of-mass kinetic energy, the simulated rovibronic spectra have transition linewidths, Δv, at T = 500 K, of ~400 MHz (cyan line). At 30 keV, the linewidths can be reduced by up to three orders of magnitude (magenta line), limited by the natural linewidth of the transition. **d**, A spectrum of our current results (red and grey lines) is compared with previous results (blue dots)[17], displaying the linewidth reduction from ~60 GHz to ~150 MHz. The x axis shows the wavenumber of the first-step laser in cm^{-1}. The y axis shows the ion count rate in arbitrary units (a.u.). The error bars represent one standard deviation statistical uncertainty.

Due to their close-lying rotational states of opposite parity, molecules can be imbued with an enhanced sensitivity, of more than 11 orders of magnitude, to symmetry-violating properties, relative to atoms[5,6]. In addition, as the strength of symmetry-violating effects rapidly scales with atomic number, nuclear spin and nuclear deformation, molecules containing heavy, radioactive nuclei, such as the pear-shaped radium (Ra)[10], are predicted to further provide more than two orders of magnitude enhancement, relative to non-radioactive systems[11–16].

Radium monofluoride (RaF) molecules are particularly attractive systems to study the aforementioned physical phenomena, as their molecular structure has been suggested to be favourable for laser cooling, paving the way towards highly sensitive studies, and a diverse range of opportunities in fundamental physics research[13,17–19]. However, in contrast to atoms, laser-cooling molecules is substantially more complex. Due to their rotational and vibrational degrees of freedom, finding appropriate cycling transitions for laser cooling poses a major experimental challenge[20–27].

Here we performed precision studies of the rovibronic structure of ^{226}Ra^{19}F. We present a three-step resonance ionization scheme that allows very sensitive measurements with a high rotational-state selectivity, while also improving the spectral resolution of our measurements by more than two orders of magnitude (Fig. 1d) with respect to previous experiments[17,19]. This allowed for precise measurements of the structure of these molecules and their energy levels that are suitable for fundamental physics studies. By employing a combination of narrow- and broad-band laser systems, we were able to address molecules in specific rotational levels, populated with yields as low as a few hundred per second, and immersed within a highly congested spectrum. Our achieved combination of experimental resolution, high sensitivity and low background is critical for the study of radioactive molecules, which are produced with small fluxes (<10^6 molecules per s), high temperatures (>2,000 K) and in contaminated environments. Additionally, our results provide an unambiguous identification and quantification of a laser cooling scheme of this molecule, which can be achieved by using only three lasers. This is an essential step towards achieving ultra-cold temperatures and performing symmetry-violating measurements with these molecules in dedicated future experiments.

Isotopes of radium were produced by impinging 1.4-GeV protons onto a uranium-carbide target. Following reactions with a CF$_4$ gas introduced into the target container, RaF$^+$ molecules were formed, extracted, mass separated and injected into a room-temperature radio-frequency trap, filled with He gas, which cooled and bunched them. Bunches of RaF$^+$, accelerated to 29.908(1) keV, were then sent towards the Collinear Resonance Ionization Spectroscopy (CRIS) setup at the Isotope Separator On Line Device Radioactive Ion Beam Facility at the European Organization for Nuclear Research (ISOLDE-CERN)[17,19,28] once every 20 ms. The high translational energy of the molecular bunch allows a significant reduction of the transitions' linewidth (Fig. 1c)[29,30]. The ions were neutralized in-flight by passing through a charge-exchange cell filled with a sodium vapour at a temperature of ~500 K, predominantly populating the X$^2\Sigma^+$ electronic ground state in the neutralization process[17,19]. The remaining ions were deflected from the neutral beam, which was then collinearly overlapped with three pulsed laser beams in an ultra high-vacuum (5 × 10^{-10} mbar) interaction region (Fig. 1a). Further details of the experimental setup can be found in Methods.
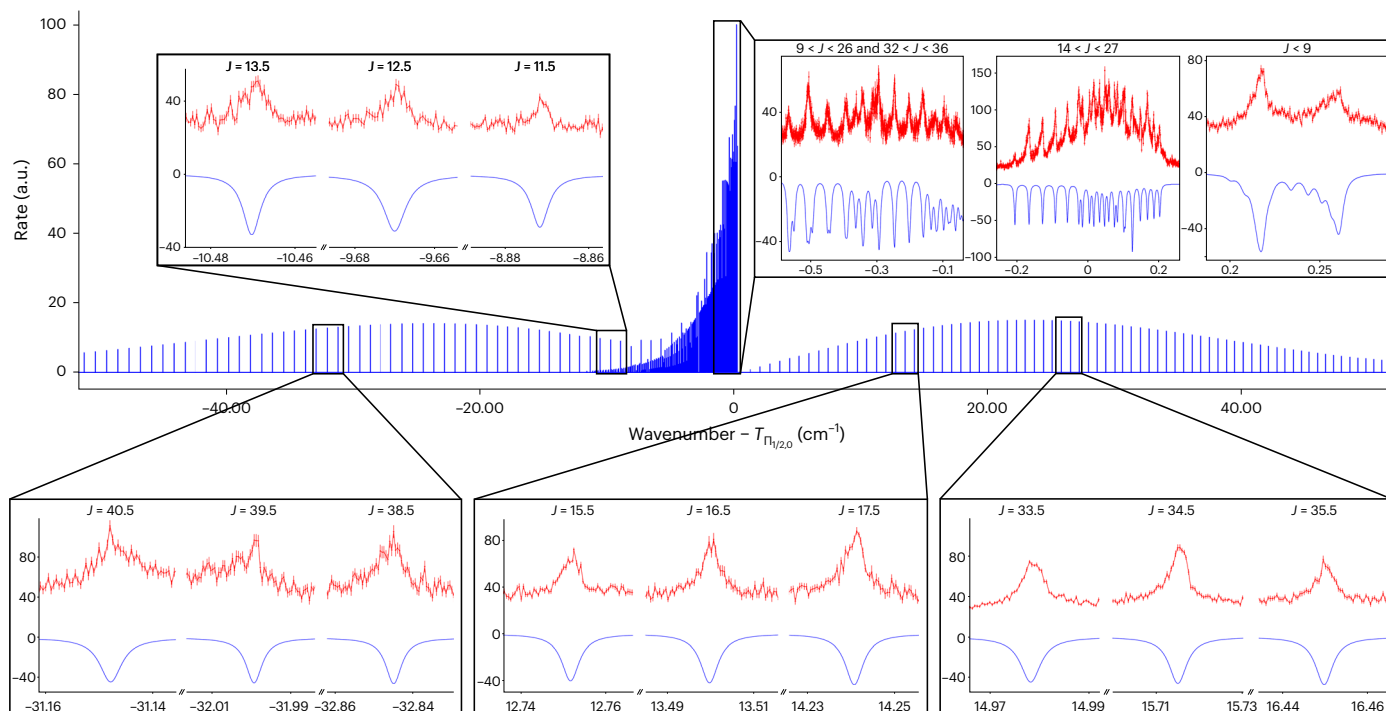
Fig. 2 | Example of measured spectra for the $0' \leftarrow 0''$ transitions. In the centre, in blue, we present the simulated RaF rovibronic spectrum obtained for $J \leq 100$, over a range of ~100 cm^{-1} (J is the rotational quantum number of the rotational levels in the X$^2\Sigma^+$ electronic level). Figures in magnified views show measured spectra for different regions (note the broken x axis present in some of the figures). The connected red dots show the experimental data, whereas the continuous blue line represents the best fit to the data. The error bars indicate one standard deviation statistical uncertainty. For each spectrum, we also show the covered range of J values (see the main text and Methods for the details of the fit). The values on the x axis correspond to the wavenumber of the first laser used in the excitation-ionization scheme, Doppler-corrected to the molecular rest frame and shifted by $T_{\Pi_{1/2},0} = 13284.427$ cm^{-1}. The rate on the y axis is given in arbitrary units (a.u.).

The RaF molecules were resonantly ionized by a stepwise three-photon process. Firstly, an injection-seeded Titanium:Sapphire (Ti:Sa) laser of tunable wavelength, with a linewidth of 20 MHz, was used to resonantly excite the rovibronic transitions of interest, between the vibrational ground or first-excited states of X$^2\Sigma^+$ and A$^2\Pi_{1/2}$, denoted as $0' \leftarrow 0''$ and $1' \leftarrow 1''$, respectively. Then, a tunable pulsed dye laser, with a linewidth of 10 GHz and wavenumber around 15,500 cm^{-1} (645 nm), resonantly excited molecules in the A$^2\Pi_{1/2}$ state to a higher-lying electronic state, tentatively assigned as a $^2\Pi_{1/2}$ (ref. 31) (an example of the spectra of the seconds step transition is shown in Extended Data Fig. 1). Finally, the electronically excited RaF molecules were ionized using a high-power (40 mJ per pulse) neodymium-doped yttrium-aluminium-garnet pulsed laser (Nd:YAG) at 532 nm (Fig. 1b). For a given wavelength of the first laser, the second laser wavelength, as well as the timing of the three lasers, were adjusted to maximize the measured ion signal. Resonant excitation to the higher-lying $^2\Pi_{1/2}$ electronic state, that lies closer to the ionization potential, enabled a longer-wavelength non-resonant laser to be used for the ionization step in this three-step scheme. This significantly reduced the non-resonant laser background, increasing the signal-to-noise ratio by an order of magnitude, compared to a two-step scheme[17,19], and facilitating an almost three orders of magnitude improved spectroscopic resolution.

The resonantly ionized RaF$^+$ molecules were deflected from the neutral bunch and detected by a MagneTOF ion detector. The wavelength of the ionization laser was chosen such that RaF molecules can only be ionized if they exist in the intermediate highly-excited electronic state, that is if the frequency of the first- and second-step lasers were on resonance with sequential transitions in the RaF molecule. The rovibronic spectra were obtained by counting the number of detected ions as a function of the wavelength of the first laser.

Figure 2 shows examples of experimental spectra, where the data are shown as red points and the fitted peak positions are shown in blue (similar spectra for the $1' \leftarrow 1''$ transitions, as well as more details about the $0' \leftarrow 0''$ transitions are shown in Extended Data Fig. 2 and Extended Data Fig. 3, respectively). In the centre, in blue, we show the full simulated spectrum of RaF for $J \leq 100$ and $T = 500$ K, over a range of ~100 cm^{-1} (J represents the rotational quantum number of the rotational levels in the X$^2\Sigma^+$ electronic level and T represents the temperature). For each measured spectrum, we also indicate the range of J values contained within it. The x axis shows the wavenumber of the first excitation laser, Doppler-corrected to the molecular rest frame and shifted by $T_{\Pi_{1/2},0} = 13284.427$ cm^{-1}. The temperature of the simulations was estimated based on the distribution of the population of the rotational levels in the $0' \leftarrow 0''$ vibrational spectrum. At this temperature, no states with $J > 100$ are expected to be observed in our experiment. However, the extraction of the physical parameters from the data depends only on the location of the measured transitions in frequency space and not on their intensity. Therefore, the obtained results are not affected by the choice of temperature.

We fitted the $0' \leftarrow 0''$ and $1' \leftarrow 1''$ transitions using an effective rotational Hamiltonian for each of the two electronic states. The fit was performed using the publicly available software PGOPHER[32]. For the fit, we used 60 spin-rotation transitions with values of J ranging from 1.5 to 40.5 for $0' \leftarrow 0''$ and 32 spin-rotation transitions with J values from 5.5 to 36.5 for $1' \leftarrow 1''$. The values of the molecular parameters obtained from the fitting procedure are shown in the second and third column of Table 1, for the $v = 0$ and $v = 1$ vibrational levels of the X$^2\Sigma^+$ and A$^2\Pi_{1/2}$ states, respectively (the resulting vibrational independent parameters are shown in Extended Data Table 1). A comparison with theoretical predictions, where available, is displayed in the last column.

Table 1 | Fitted rotational parameters

| Parameter	$v=0$ (cm^{-1})	$v=1$ (cm^{-1})	Theory[a] (cm^{-1})
B''_v	0.191985(5)[15]	0.19092(4)[6]	0.192[b]
			0.1909[c]
$10^7 \times D''_v$	1.40(5)[10]	1.2(3)[4]	
γ_v	0.00585(3)[7]	0.00581(5)[15]	0.006[d]
B'_v	0.191015(5)[15]	0.18997(4)[6]	0.192[b]
			0.1902[c]
$10^7 \times D'_v$	1.40(5)[10]	1.5(3)[4]	
p_v	−0.41071(3)[7]	−0.40978(10)[20]	
$10^7 \times p_{D,v}$	1.9(2)[5]	4.4(20)[15]	
$T_{\Pi_{1/2},v}$	13284.427(1)[20]	13278.316(1)[20]	13300[c]

In the first column, we list the parameter names, while the second and third columns show their values for the ground and first-excited vibrational states of the X$^2\Sigma^+$ and A$^2\Pi_{1/2}$ electronic manifolds. We show the 1σ statistical and systematic uncertainties in round and square brackets, respectively. In the last column we present the available theoretical predictions.
[a] The theoretical studies report the equilibrium rotational parameters: $B_e \approx \frac{3}{2}B_0 - \frac{1}{2}B_1$ and $\gamma_e \approx \frac{3}{2}\gamma_0 - \frac{1}{2}\gamma_1$. [b] Ref. 14 [c] Ref. 33 [d] Ref. 34

An excellent agreement is seen between the experimentally determined values and previous ab initio calculations[14,33,34]. A detailed description of the data analysis, as well as an in-depth explanation of the effective Hamiltonians employed, are presented in Methods.

In Fig. 3, we show a laser cooling scheme for RaF, requiring only three lasers. The location of the relevant spin-rotational levels in frequency space was obtained from the fitted rotational parameters. The Franck–Condon factors, $f_{v',v''}$, between the X$^2\Sigma^+$ and A$^2\Pi_{1/2}$ vibrational levels were calculated assuming a Morse potential for each of the two electronic states, parameterized using the rotational constants obtained in this work, B'_e and B''_e (Methods), as well as the vibrational constants and dissociation energies from ref. 17. The solid, upwards-pointing arrows represent laser excitations, while the sinusoidal ones represent spontaneous emission. One laser will be used to pump the main cooling transitions between the $J^P = 0.5^-$, $v = 0$ and $J^P = 1.5^-$, $v = 0$ levels of the X$^2\Sigma^+$ state and the $J^P = 0.5^+$, $v = 0$ level of the A$^2\Pi_{1/2}$ state (the '+' and '−' refer to the parity of the state, P). The use of these spin-rotational states will eliminate rotational branching, as described in ref. 20. Given that the two levels in the X$^2\Sigma^+$ are separated by 263(4) MHz, a single laser with modulated frequency would be able to address both of them simultaneously. Two other lasers are used to re-pump molecules that decay to the $v = 1$ and $v = 2$ vibrational levels of the X$^2\Sigma^+$ state, back into the main cooling cycle. The described approach would allow each molecule to scatter more than 10^5 photons on average before it ends up in a dark state, at a rate greater than 10^6 photons per second (given by the lifetime of the excited A$^2\Pi_{1/2}$ state, $\tau < 50$ ns)[17].

While previous low-resolution measurements presented evidence for the existence of a laser cooling scheme of RaF[17], our results quantitatively provide the spin-rotation levels suitable for such a scheme, as well as the associated Franck–Condon factors, facilitating an unambiguous pathway to laser-cooling this molecule. This will allow future experimental developments aiming to laser cool and trap RaF molecules for fundamental physics studies[8]. In order to achieve laser cooling over reasonably short distances, as well as increase the population in the relevant rotational levels, developments of efficient production methods of cold RaF beams are needed[35]. Compared to other alkaline-earth monohalides, RaF is, to our knowledge, the most favourable molecule for laser cooling, in terms of the diagonality of Franck–Condon factors[20] and relatively simple energy-levels structure. The absence of any electronic manifolds between the two electronic states used for laser
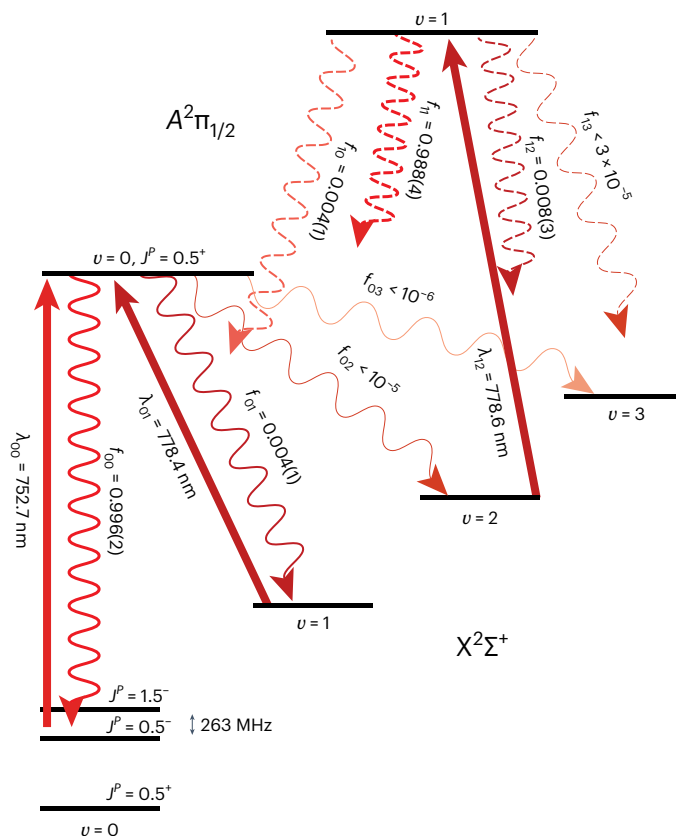

Fig. 3 | Proposed laser cooling scheme for RaF. The upwards-pointing arrows represent laser excitations between the ground, X$^2\Sigma^+$, and excited, A$^2\Pi_{1/2}$, electronic states. The wavelength of each laser ($\lambda_{v'v''}$) is shown (energy levels not shown to scale). The wavy, downwards-pointing arrows represent spontaneous emission from the $v' = 0$ (continuous lines) and $v' = 1$ (dashed lines) vibrational levels, including the associated Franck–Condon factors ($f_{v'v''}$). The labels v' and v'' represent the vibrational quantum number of the excited and ground electronic manifolds, respectively. The vibrational (v) and rotational (J) quantum numbers as well as the parity (+/−) are shown for the states of interest. Similar colours indicate similar values of the transition frequencies. We show in brackets the uncertainty associated with the calculated Franck–Condon factors (see Methods for details).

cooling in RaF, is a major advantage for laser cooling[17], in contrast to BaF (ref. 36), the heaviest stable alkaline-earth monohalide.

Due to the inherent complexity and heavy mass of RaF molecules, a large number of rovibronic transitions, originating from states with different J, can lie very close to each other. The first-step laser can therefore excite several of them simultaneously, even with a linewidth as narrow as a few tens of MHz. By properly adjusting the wavelength of the second-step laser, we introduce additional J-selectivity such that only molecules from a given initial rotational state are ionized. This enabled the observation of individual transitions with initial J values from 0.5 up to 40.5. An example of this J-selection is shown in Fig. 4 (more examples are shown in the Extended Data Fig. 4). Transitions containing J values between 0.5 and 3.5 can be isolated from a large background of higher-J transitions despite these states being populated much more strongly. In the upper part, the red dots represent the data, while the blue line is the result of a fit to the data using a sum of six peaks and a constant background. The dashed green lines show the individual fitted peaks. The same fitted spectrum is compared in the bottom part to the spectrum without the $J < 4$ cut (black dashed line). Without the additional second-step J-selectivity, the displayed wavelength region contains J values up to 15.5 (marked as the vertical black lines), making the investigation of low-J transitions virtually impossible. The rate of
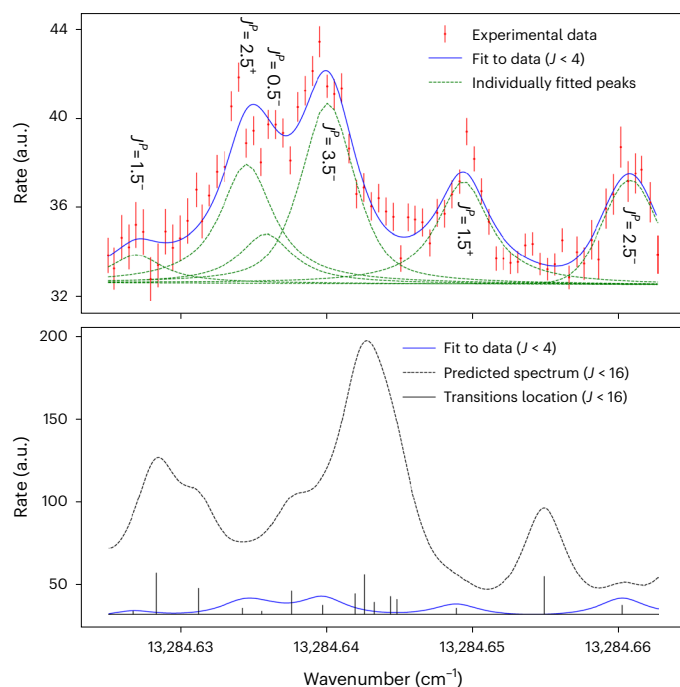
Fig. 4 | Measured spectra using second-step J-selectivity. In the upper part, the red dots represent the data while the blue continuous line is the result of a fit to the data, containing six peaks (shown in green) plus a constant background. The error bars show one standard deviation statistical uncertainty. For each peak we indicate the rotational quantum number, J and the parity of its ground rotational level. In the bottom part, the fit (blue line) is compared to the expected spectra without any cut on the J values range of the transitions (black dashed line). The black vertical lines mark the position of each transition (see the main text for the details of the fit).

molecules in the interaction region, populating states with $J < 4$ in our experiment was estimated to be between 50 and a few hundred per second. Hence, we can isolate and perform precision studies of particular transitions within a highly congested spectrum with high sensitivity, using the three-colour ionization scheme discovered herein.

Precision experiments using ^{226}RaF molecules, as well as the extension of such experiments to molecules containing Ra isotopes with nuclear spin larger than zero, such as ^{223,225}RaF, will enable highly sensitive studies of electroweak nuclear and leptonic properties. This will include searches for parity violation, through nuclear anapole moment measurements and combined parity and time-reversal violation searches, through investigations of the electron electric dipole moment, nuclear Schiff moment and nuclear magnetic quadrupole moment[5]. Such measurements can be performed using the lowest rotational and hyperfine levels of the ground electronic state[6,9].

The accuracy achieved in our experiment approaches what is required to guide astrophysical observations of radioactive molecules of importance in our understanding of stellar nucleosynthesis and astrochemistry, such as ^{26}AlF (ref. [37]), ^{26}AlO (ref. [38]) or ^{32}SiO (refs. [39],[40]). The rotational de-excitations of these molecules can be sensitively observed with a high spatial resolution using modern telescope facilities[41,42]. However, their identification requires a very precise knowledge of their rotational structure which can only be unambiguously obtained from laboratory measurements, achievable with the technique presented here.

In addition, several other radioactive molecules are predicted to possess an enhanced sensitivity to fundamental symmetry violations, such as RaOH (ref. [43]), RaO (ref. [12]), RaH (ref. [44]), RaOCH$_3^+$ (refs. [45],[46]), PaF^{3+} (ref. [47]) or AcOH$^+$ (ref. [48]). However, their structure remains experimentally unknown. The described measurement technique can

be used to investigate these and other short-lived radioactive molecules of fundamental physics interest. The extension of our current method to polyatomic molecules poses additional challenges, as extra degrees of freedom come into play. Further improvements in the resolution of the first-step transition (Methods), as well as the possibility of using the second-step laser to isolate individual transitions from complex molecular spectra, as described in this work, could allow the investigation of such species. The developments presented in this work are timely with respect to the current efforts to produce radioactive molecules for fundamental physics research at different facilities worldwide such as ISOLDE-CERN (Switzerland), the TRI-University Meson Facility (TRIUMF) (Canada), and the Facility for Rare Isotope Beams (FRIB) (US)[8].

Online content

Any methods, additional references, Nature Portfolio reporting summaries, source data, extended data, supplementary information, acknowledgements, peer review information; details of author contributions and competing interests; and statements of data and code availability are available at https://doi.org/10.1038/s41567-023-02296-w.

References

1. Tanabashi, M. et al. Review of particle physics: particle data groups. *Phys. Rev. D* **98**, 030001 (2018).
2. Hudson, J. J. et al. Improved measurement of the shape of the electron. *Nature* **473**, 493–496 (2011).
3. ACME collaboration. Order of magnitude smaller limit on the electric dipole moment of the electron. *Science* **343**, 269–272 (2014).
4. Cairncross, W. B. et al. Precision measurement of the electron's electric dipole moment using trapped molecular ions. *Phys. Rev. Lett.* **119**, 153001 (2017).
5. Safronova, M. S. et al. Search for new physics with atoms and molecules. *Rev. Mod. Phys.* **90**, 025008 (2018).
6. Altuntaş, E. et al. Demonstration of a sensitive method to measure nuclear-spin-dependent parity violation. *Phys. Rev. Lett.* **120**, 142501 (2018).
7. ACME Collaboration. Improved limit on the electric dipole moment of the electron. *Nature* **562**, 355–360 (2018).
8. Arrowsmith-Kron, G. et al. Opportunities for fundamental physics research with radioactive molecules. Preprint at *arXiv* https://doi.org/10.48550/arXiv.2302.02165 (2023).
9. Roussy, T. S. et al. An improved bound on the electron's electric dipole moment. *Science* **381**, 46–50 (2023).
10. Gaffney, L. P. et al. Studies of pear-shaped nuclei using accelerated radioactive beams. *Nature* **497**, 199–204 (2013).
11. Auerbach, N., Flambaum, V. V. & Spevak, V. Collective T-and P-odd electromagnetic moments in nuclei with octupole deformations. *Phys. Rev. Lett.* **76**, 4316–4319 (1996).
12. Flambaum, V. V. Electric dipole moments of actinide atoms and RaO molecule. *Phys. Rev. A* **77**, 024501 (2008).
13. Isaev, T. A., Hoekstra, S. & Berger, R. Laser-cooled RaF as a promising candidate to measure molecular parity violation. *Phys. Rev. A* **82**, 052521 (2010).
14. Kudashov, A. D. et al. Ab initio study of radium monofluoride (RaF) as a candidate to search for parity-and time-and-parity–violation effects. *Phys. Rev. A* **90**, 052513 (2014).
15. Sasmal, S., Pathak, H., Nayak, M. K., Vaval, N. & Pal, S. Relativistic coupled-cluster study of RaF as a candidate for the parity-and time-reversal-violating interaction. *Phys. Rev. A* **93**, 062506 (2016).
16. Gaul, K., Marquardt, S., Isaev, T. & Berger, R. Systematic study of relativistic and chemical enhancements of P, T-odd effects in polar diatomic radicals. *Phys. Rev. A* **99**, 032509 (2019).
17. Garcia Ruiz, R. F. et al. Spectroscopy of short-lived radioactive molecules. *Nature* **581**, 396–400 (2020).

18. Isaev, T.A. & Berger, R. Lasercooled radium monofluoride: a molecular all-in-one probe for new physics. Preprint at *arXiv* https://doi.org/10.48550/arXiv.1302.5682 (2013).

19. Udrescu, S. M. et al. Isotope shifts of radium monofluoride molecules. *Phys. Rev. Lett.* **127**, 033001 (2021).

20. Shuman, E. S., Barry, J. F. & DeMille, D. Laser cooling of a diatomic molecule. *Nature* **467**, 820–823 (2010).

21. Barry, J. F., McCarron, D. J., Norrgard, E. B., Steinecker, M. H. & DeMille, D. Magneto-optical trapping of a diatomic molecule. *Nature* **512**, 286–289 (2014).

22. Truppe, S. et al. Molecules cooled below the Doppler limit. *Nat. Phys.* **13**, 1173–1176 (2017).

23. Kozyryev, I. et al. Sisyphus laser cooling of a polyatomic molecule. *Phys. Rev. Lett.* **118**, 173201 (2017).

24. Anderegg, L. et al. Laser cooling of optically trapped molecules. *Nat. Phys.* **14**, 890–893 (2018).

25. Lim, J. et al. Laser cooled YbF molecules for measuring the electron's electric dipole moment. *Phys. Rev. Lett.* **120**, 123201 (2018).

26. Mitra, D. et al. Direct laser cooling of a symmetric top molecule. *Science* **369**, 1366–1369 (2020).

27. Jorapur, V., Langin, T.K., Wang, Q., Zheng, G. & DeMille, D. High density loading and collisional loss of laser cooled molecules in an optical trap. Preprint at *arXiv* https://doi.org/10.48550/arXiv.2307.05347 (2023).

28. Catherall, R. et al. The ISOLDE facility. *J. Phys. G* **44**, 094002 (2017).

29. Campbell, P., Moore, I. D. & Pearson, M. R. Laser spectroscopy for nuclear structure physics. *Prog. Part. Nucl. Phys.* **86**, 127–180 (2016).

30. Yang, X. F., Wang, S. J., Wilkins, S. G. & Garcia Ruiz, R. F. Laser spectroscopy for the study of exotic nuclei. *Prog. Part. Nucl. Phys.* **129**, 104005 (2022).

31. Athanasakis-Kaklamanakis, M. et al. Pinning down electron correlations in RaF via spectroscopy of excited states. Preprint at *arXiv* https://doi.org/10.48550/arXiv.2308.14862 (2023).

32. Western, C. M. PGOPHER: a program for simulating rotational, vibrational and electronic spectra. *J. Quant. Spectrosc. Radiat. Transf.* **186**, 221–242 (2017).

33. Zaitsevskii, A. et al. Accurate ab initio calculations of RaF electronic structure appeal to more laser-spectroscopical measurements. *J. Chem. Phys.* **156**, 044306 (2022).

34. Petrov, A. N. & Skripnikov, L. V. Energy levels of radium monofluoride RaF in external electric and magnetic fields to search for P-and T, P-violation effects. *Phys. Rev. A* **102**, 062801 (2020).

35. Hutzler, N. R., Lu, H. I. & Doyle, J. M. The buffer gas beam: an intense, cold, and slow source for atoms and molecules. *Chem. Rev.* **112**, 4803–4827 (2012).

36. Aggarwal, P. et al. Measuring the electric dipole moment of the electron in BaF. *Eur. Phys. J. D*, **72**, 197 (2018).

37. Kamiński, T. et al. Astronomical detection of radioactive molecule ^{26}AlF in the remnant of an ancient explosion. *Nat. Astron.* **2**, 778–783 (2018).

38. Chubb, K. L., Min, M., Kawashima, Y., Helling, C. & Waldmann, I. Aluminium oxide in the atmosphere of hot Jupiter WASP-43b. *Astron. Astrophys.* **639**, A3 (2020).

39. Fujiya, W., Hoppe, P., Zinner, E., Pignatari, M. & Herwig, F. Evidence for radiogenic sulfur-32 in type AB presolar silicon carbide grains? *Astrophys. J. Lett.* **776**, L29 (2013).

40. Cairnie, M., Forrey, R. C., Babb, J. F., Stancil, P. C. & McLaughlin, B. M. Rate constants for the formation of SiO by radiative association. *Mon. Notices Royal Astron. Soc.* **471**, 2481–2490 (2017).

41. Lacy, J. H., Richter, M. J., Greathouse, T. K., Jaffe, D. T. & Zhu, Q. Texes: a sensitive high-resolution grating spectrograph for the mid-infrared. *Publ. Astron. Soc. Pac.* **114**, 153–168 (2002).

42. Fomalont, E. B. et al. The 2014 ALMA long baseline campaign: an overview. *Astrophys. J. Lett.* **808**, L1 (2015).

43. Isaev, T. A., Zaitsevskii, A. V. & Eliav, E. Laser-coolable polyatomic molecules with heavy nuclei. *J. Phys. B* **50**, 225101 (2017).

44. Fazil, N. M., Prasannaa, V. S., Latha, K. V. P., Abe, M. & Das, B. P. RaH as a potential candidate for electron electric-dipole-moment searches. *Phys. Rev. A* **99**, 052502 (2019).

45. Yu, P. & Hutzler, N. R. Probing fundamental symmetries of deformed nuclei in symmetric top molecules. *Phys. Rev. Lett.* **126**, 023003 (2021).

46. Fan, M. et al. Optical mass spectrometry of cold RaOH$^+$ and RaOCH$_3^+$. *Phys. Rev. Lett.* **126**, 023002 (2021).

47. Zülch, C., Gaul, K., Giesen, S. M., Ruiz, R. F. G. & Berger, R. Cool molecular highly charged ions for precision tests of fundamental physics. Preprint at *arXiv* https://doi.org/10.48550/arXiv.2203.10333 (2022).

48. Oleynichenko, A. V., Skripnikov, L. V., Zaitsevskii, A. V. & Flambaum, V. V. Laser-coolable AcOH$^+$ ion for CP-violation searches. *Phys. Rev. A* **105**, 022825 (2022).

Methods

For this experiment, radium isotopes were produced by imping-ing 1.4-GeV protons onto a thick uranium-carbide target. By inject-ing CF_4 gas through a calibrated leak into the target container, radium-containing molecules were formed. Through surface ioni-zation, RaF^+ was created and extracted using an electrostatic field. The isotopologue of interest for the present study, $^{226}Ra^{19}F^+$, was mass-selected using a high-resolution magnetic mass separator and then collisionally cooled in a radio-frequency quadrupole trap filled with room-temperature helium gas for up to 20 ms. After that, bunches of $^{226}Ra^{19}F^+$ were released, accelerated to an energy of 29.908(1) keV, and then sent to the Collinear Resonance Ionization Spectroscopy setup[49–53]. The energy of the molecular bunch allows a significant reduction of the measured transitions' linewidths[29,30]. This is possible because, during the acceleration, the initial energy spread of the ions is preserved, while their velocity increases, which leads to a reduc-tion of the ion beam velocity spread along its axis of motion. At our acceleration voltage, the linewidths of the measured transitions can be reduced by up to three orders of magnitude, compared to a meas-urement performed on a thermal beam[29,30]. In practice, the observed linewidths are broader than this due to power broadening, variations in the acceleration voltage, collisions in the charge-exchange cell and the linewidth of the spectroscopy laser used. Reducing these effects will improve the resolution of the measured spectra.

Measured and fitted spectra, corresponding to $1' \leftarrow 1''$ rovibronic transitions, are presented in Extended Data Fig. 2, together with the rotational quantum numbers, J, that they contain. In the centre, we show the fitted spectrum simulated in PGOPHER for $J \leq 100$ and $T = 500$ K, over a region of ~70 cm^{-1}. The magnified views show different regions of the spectrum, with the red dots representing measured data, and the blue continuous line showing the best fit to the data. The x axis shows the wavenumber of the first-step laser, Doppler-corrected to the molecular rest frame and shifted by $T_{\Pi_{1/2},0} = 13284.427$ cm^{-1}. The y axis shows the rate in arbitrary units. During the experiment, the wave-length of the first-step Ti:Sa laser was measured with a wavemeter (WSU-2, HighFinesse) calibrated by measuring a reference wavelength provided by a rubidium-stabilized diode laser (DLC DL PRO 780, Top-tica)[17]. Simultaneously, we measured the $5^2S_{1/2}, F = 2 \rightarrow 5^2P_{3/2}, F = 3$ transition in ^{87}Rb with the same wavemeter, as a reference, in order to correct for any measurement drifts. The wavenumbers shown in Fig. 2 and in Extended Data Fig. 2 were calculated using:

$$\tilde{v} = \tilde{v}_m - \left(\tilde{v}_m^{Rb} - \tilde{v}_0^{Rb}\right) \tag{1}$$

where $\tilde{v}_m$ and $\tilde{v}_m^{Rb}$ are the measured wavenumbers of the Ti:Sa laser and of the ^{87}Rb transition, respectively, while $\tilde{v}_0^{Rb}$ is the literature value of the reference ^{87}Rb transition[54]. Each peak used for the determination of the rotational Hamiltonian was fit with a Voigt profile plus a constant back-ground, using the LMFIT Python package[55]. The number of peaks in a given scan was chosen based on the reduced χ^2 of the fit. The obtained central value of each peak, together with its associated uncertainty, were used as input in PGOPHER, in order to extract the rotational parameters.

The main sources of systematic uncertainties in our experimen-tal setup were (the associated uncertainty in the measured wave-number is given in brackets): variations in the ion beam's extraction voltage (1.2×10^{-4} cm^{-1}), changes in the beam energy during the charge-exchange process (<10^{-4} cm^{-1}), uncertainties in the measure-ment of the Rb reference frequency by the wavemeter (10^{-4} cm^{-1}), pres-ence of stray magnetic and electric fields (<10^{-5} cm^{-1}) and AC Stark shifts due to the presence of the second- and third-step lasers (5×10^{-4} cm^{-1}). These uncertainties were added to the statistical uncertainty for each fitted line in the spectra, before performing the PGOPHER fit.

For the simulation of the spectrum in PGOPHER, the vibrational levels in the electronic ground state, $X^2\Sigma^+$, were described by the effec-tive Hund's case (b) Hamiltonian:

$$H_{X^2\Sigma^+} = (B'' - D''\mathbf{N}^2)\mathbf{N}^2 + \gamma\mathbf{N}\cdot\mathbf{S} \tag{2}$$

where B'' is the rotational constant, D'' is the centrifugal distortion constant and γ is the spin-rotation constant. $\mathbf{N} = \mathbf{J} - \mathbf{S}$ and $\mathbf{S}$ are the molecular-rotational operator (excluding the electron spin) and electron-spin operator, respectively. The vibrational levels in the excited electronic state, $A^2\Pi$, were described by the effective Hund's case (a) Hamiltonian:

$$H_{A^2\Pi} = T_\Pi - \frac{A_\Pi}{2} + (B' - D'\mathbf{N}^2)\mathbf{N}^2 -$$
$$- \frac{1}{4}\{p + p_D\mathbf{N}^2, N_+S_+e^{-2i\phi} + N_-S_-e^{2i\phi}\} \tag{3}$$

where $\{O,Q\} = OQ + QO$, T_Π represents the distance between the origins of the $v' = 0$ and $v' = 1$ vibrational levels of the $^2\Pi$ electronic manifold and the origins of the corresponding isovibrational levels of the $X^2\Sigma^+$ electronic manifold, while A_Π is the spin–orbit interaction. As rovi-bronic transitions to the $A^2\Pi_{3/2}$ electronic state were not measured, it wasn't possible to constrain both T_Π and A_Π simultaneously so A_Π was kept fixed at its previously measured value of 2067.6 cm^{-1} (ref. 17). p is the Λ-doubling parameter and p_D is the centrifugal distortion correc-tion to p. $N_\pm$ and $S_\pm$ are the raising and lowering operators for the $\mathbf{N}$ and $\mathbf{S}$ operators defined above and ϕ is the electron orbital azimuthal angle. Because of the coupling between the rotation of the molecule and the electron orbital angular momentum, each level with a given quantum number J is split into two levels of opposite parity. Note that the terms in the Hamiltonians above are effective parameters, which include the small contributions of the other electronic states in the molecule[56]. The hyperfine splitting due to the fluorine nucleus is expected to be less than 100 MHz (ref. 33) and we were not able to observe this effect given our experimental resolution. The associated hyperfine Hamil-tonian was therefore not included in the analysis. For laser cooling, the ground-state hyperfine sublevels of interest can be addressed using sidebands obtained from the modulation of the frequency of the laser used to pump the main cooling transition, similar to other laser-cooled molecules[20]. This will not influence the number of lasers needed, their frequencies or the calculated Franck–Condon factors.

From equations (2) and (3) we can see that in total there are nine parameters that we need to fit for, three for the ground and six for the excited state. Given the large parameter space, choosing initial values for the fit as close as possible to the true ones was crucial. It was also impor-tant to reduce the number of free parameters by using (approximate) theoretically and experimentally motivated constraints between them. These constraints were used only in the beginning of the fitting proce-dure, in order to have a fast convergence towards an optimal region of the parameter space. The only exception was for the A_Π parameter which was kept fixed at its previously measured value of 2,067.6 cm^{-1} (ref. 17).

We started the fitting procedure with $0' \leftarrow 0''$ rovibronic transi-tions. The rotational constants, B, of the $X^2\Sigma^+$ and $A^2\Pi_{1/2}$ electronic states were calculated in ref. 14 to be equal to 0.192 cm^{-1}. Based on the spacing between the well-separated measured peaks (located on the left and right side of the spectrum shown in Fig. 2), we were able to obtain two approximate constraints using combination differences:

$$B'' - B' = 0.001 \text{ } cm^{-1}$$
$$p = 6B' - \gamma - 1.552 \text{ } cm^{-1} \tag{4.}$$

Hence, we set the initial rotational constants to $B'' = 0.192$ cm^{-1} and $B' = 0.191$ cm^{-1}. The initial value of T_Π was initially set to 14315 cm^{-1}, according to ref. 17, while γ was set to 0.006 cm^{-1} (ref. 33). For a Morse potential, the centrifugal distortion constant can be written in terms of the rotational constant as:

$$D = \frac{4B^3}{\omega^2} \tag{5}$$

where ω is the vibrational constant of the electronic level, which in our case for the $X^2\Sigma^+$ and $A^2\Pi_{1/2}$ states it is equal to $\omega_{X^2\Sigma^+} = 441.8$ cm^{-1} and $\omega_{A^2\Pi_{1/2}} = 435.5$ cm^{-1} (ref. [17]). Together with the values of the rotational constants considered above, the initial values for the centrifugal distortion constants were set to: $D'' = 1.45 \times 10^{-7}$ cm^{-1} and $D' = 1.47 \times 10^{-7}$ cm^{-1}. Initially p_D was set to zero.

Using these initial values of the parameters, we were able to assign the two bandheads present in the simulations and in the data to their respective transition branches. The location of the bandheads for the $0' \leftarrow 0''$ transitions is indicated with green arrows in the spectrum shown in Extended Data Fig. 3. Red dots represent the data, while the blue line is the fit to the data. The x axis corresponds to the wavenumber of the first laser used in the excitation-ionization scheme, Doppler-corrected to the molecular rest frame and shifted by $T_{\Pi_{1/2},0} = 13284.427$ cm^{-1}. The y axis shows the rate in arbitrary units. This made the assignment of the measured transitions to the right branches substantially easier.

The fitting procedure started with only two free parameters: the rotational constant of the ground state, B'', and the centre of the excited state, T_Π. In PGOPHER, each measured transition is assigned to the closest transition in the simulated spectrum. Initially, only isolated lines, from the right and left sides of the simulated spectrum shown in Fig. 2, were used for the fit, as the assignment between the measured and simulated spectra was relatively easy. We then gradually removed the initial constraints, hence allowing other rotational parameters to vary, and we also added lines from the congested regions of the spectrum to the fit. In the end, all the molecular parameters were set as free parameters and 60 rovibronic transitions were used for the fit. For certain scans, extra peaks were present in the simulated spectrum relative to the measured ones. These extra peaks could be removed by placing simple cuts on the range of J values used in the simulation (as shown in Fig. 2), depending on the frequency of the second-step laser. We concluded that this effect is a consequence of the second-step J-selectivity described in the current work. An example of this effect is shown in Extended Data Fig. 4. We show three measurements (scans of the first-step laser) taken with the wavenumber of the second-step laser, Doppler-shifted to the molecular rest frame, being 15485.23(2) cm^{-1}, 15485.39(2) cm^{-1} and 15485.56(2) cm^{-1}. By increasing the frequency of the second-step laser, we are able to see transitions from levels with higher J values in the $A^2\Pi_{1/2} \leftarrow X^2\Sigma^+$ spectrum, increasing the maximum value of J from $J_{max} = 25.5$ to $J_{max} = 27.5$.

The second excited state used in the measurement scheme was tentatively assigned as a $^2\Pi_{1/2}$ state[31]. This was based on the shape of the spectrum of the second-step transition, obtained by scanning the frequency of the pulsed dye laser, while the frequency of the first-step laser was kept fixed. In order to make sure a wide range of J values was covered by the first step, the narrowband injection-seeded Ti:Sa laser, seeded by a Matisse 2 TS, was replaced with a grating Ti:Sa laser with a linewidth of 2 GHz for this study[17]. An example of such a scan is shown in Extended Data Fig. 1, for a wavenumber of the first-step laser of 13285.69(2) cm^{-1} (Doppler-corrected to the molecular rest frame). The red dots represent the measured data, while the blue line is the best fit to the data obtained in PGOPHER, assuming a $^2\Pi_{1/2}$ state for the second excited state. As seen in the figure, the fit is in good agreement with data over a frequency range of more than 30 cm^{-1}.

For the $1' \leftarrow 1''$ transitions we employed the same effective Hamiltonians mentioned above. We set the initial values of the parameters to the ones obtained from the fit to the $0' \leftarrow 0''$ transitions and we only allowed B'', B', p and T_Π to vary initially (A_Π was still kept fixed at 2,067.6 cm^{-1}). After several fitting iterations in PGOPHER, we allowed all the parameters to vary, including 32 rovibronic transitions in the final fit.

The parameters obtained for $v = 0$ and $v = 1$ vibrational levels of the $X^2\Sigma^+$ and $A^2\Pi_{1/2}$ electronic levels are reported in Table 1. For the location of the vibrational levels in the excited electronic state, relative to the isovibrational levels in the ground electronic state, we defined

$T_{\Pi_{1/2}} = T_\Pi - \frac{A_\Pi}{2}$. Except for $T_{\Pi_{1/2}}$, all the other parameters have a dependence on the vibrational quantum number, v, which can be parameterized, to first order in v, as:

$$X_v = X_e - \alpha_X\left(v + \frac{1}{2}\right) \tag{6}$$

where X_e can be any of the rotational parameters considered and X_v is the extracted value of that parameter in the vibrational level v. The obtained values for X_e and α_X for all the rotational parameters are shown in Extended Data Table 1.

The locations in frequency space of the spin-rotational levels proposed for the laser cooling scheme (Fig. 3) were obtained directly from the effective Hamiltonians (equations (2) and (3)) using the fitted rotational parameters (Table 1). The associated Franck–Condon factors were calculated by approximating the ground and excited electronic states using a Morse potential (similar to ref. [20]), which is a very good approximation in diatomic molecules, especially for low-lying electronic states. The potential for each level was parameterized using the rotational parameters B_e obtained in this work (Extended Data Table 1), together with the previously measured vibrational constant and dissociation energy[17]. The uncertainty on these parameters propagates to an uncertainty in the shape of the used potential and thus, to an uncertainty in the resulting Franck–Condon factors. The uncertainties associated with (or the upper bounds to) the calculated Franck–Condon factors are displayed in Fig. 3 and correspond to a 90% confidence interval.

Data availability

The processed spectra used for the analysis and supporting the findings of these studies are provided in ref. [57]. The complete raw data is available from the corresponding authors upon request. Source data are provided with this paper.

Code availability

The Python script used for fitting individual peaks as well as a PGOPHER file containing a fitted spectra for the $0' \leftarrow 0''$ and $1' \leftarrow 1''$ rovibronic transitions are provided in ref. [57]. The code used for processing the raw data is available from the corresponding authors upon request.

References

49. Flanagan, K. T. et al. Collinear resonance ionization spectroscopy of neutron-deficient francium isotopes. *Phys. Rev. Lett.* **111**, 212501 (2013).
50. De Groote, R. P. et al. Use of a continuous wave laser and pockels cell for sensitive high-resolution collinear resonance ionization spectroscopy. *Phys. Rev. Lett.* **115**, 132501 (2015).
51. Garcia Ruiz, R. F. et al. High-precision multiphoton ionization of accelerated laser-ablated species. *Phys. Rev. X* **8**, 041005 (2018).
52. Vernon, A. R. et al. Optimising the Collinear Resonance Ionisation Spectroscopy (CRIS) experiment at CERN-ISOLDE. *Nucl. Instrum. Methods. Phys. Res. B* **463**, 384–389 (2020).
53. Ágota, K. et al. Resonance ionization schemes for high resolution and high efficiency studies of exotic nuclei at the CRIS experiment. *Nucl. Instrum. Methods Phys. Res. B* **463**, 398–402 (2019).
54. Steck, D. A. Rubidium 87 D line data, revision 2.2.1 https://steck.us/alkalidata/ (21 November 2019).
55. Newville, M. et al. LMFIT: non-linear least-square minimization and curve-fitting for Python. *Zenodo* https://doi.org/10.5281/zenodo.11813 (2014).
56. Brown, J.M. & Carrington, A. *Rotational Spectroscopy of Diatomic Molecules* (Cambridge Univ. Press, 2003).
57. Udrescu, S.M. et al. Precision spectroscopy and laser cooling scheme of a radium-containing molecule. figshare https://doi.org/10.6084/m9.figshare.23703981 (2023).

Competing interests

The authors declare no competing interests.

Additional information

Extended data is available for this paper at https://doi.org/10.1038/s41567-023-02296-w.

Supplementary information The online version contains supplementary material available at https://doi.org/10.1038/s41567-023-02296-w.

Correspondence and requests for materials should be addressed to S. M. Udrescu, S. G. Wilkins or R. F. Garcia Ruiz.

Peer review information *Nature Physics* thanks Alec Owens, Aiko Takamine and the other, anonymous, reviewer(s) for their contribution to the peer review of this work.

Reprints and permissions information is available at www.nature.com/reprints.
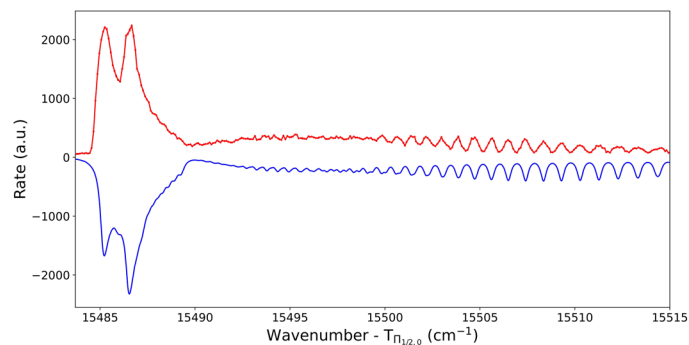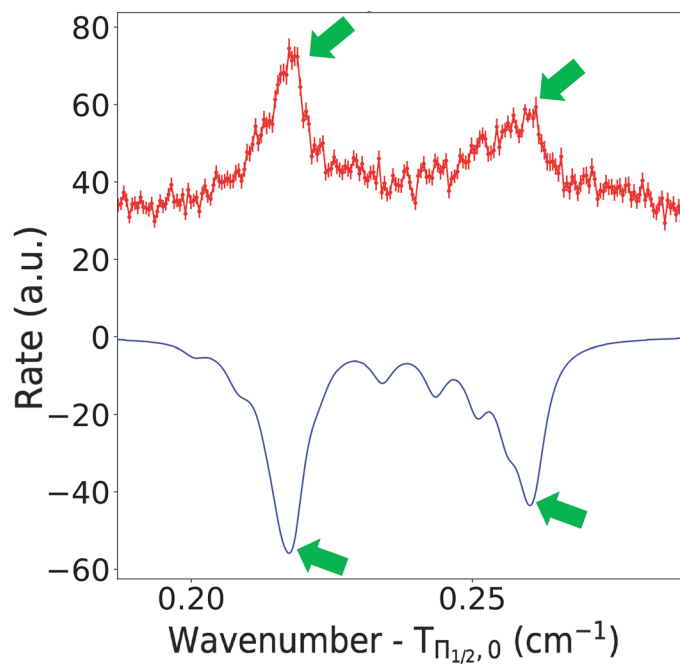
Extended Data Fig. 1 | Example of rovibronic spectra of the second step used in the experimental scheme. The red dots represent the measured data while the blue line is the best fit to the data. The x-axis corresponds to the wavenumber of the second laser used in the excitation-ionization scheme, Doppler-corrected to the molecular rest frame and shifted by $T_{\Pi_{1/2,0}} = 13284.427\,cm^{-1}$ (see Methods for the details of the fit). The y-axis shows the rate in arbitrary units (a.u.). The errorbars show one standard deviation statistical uncertainty.
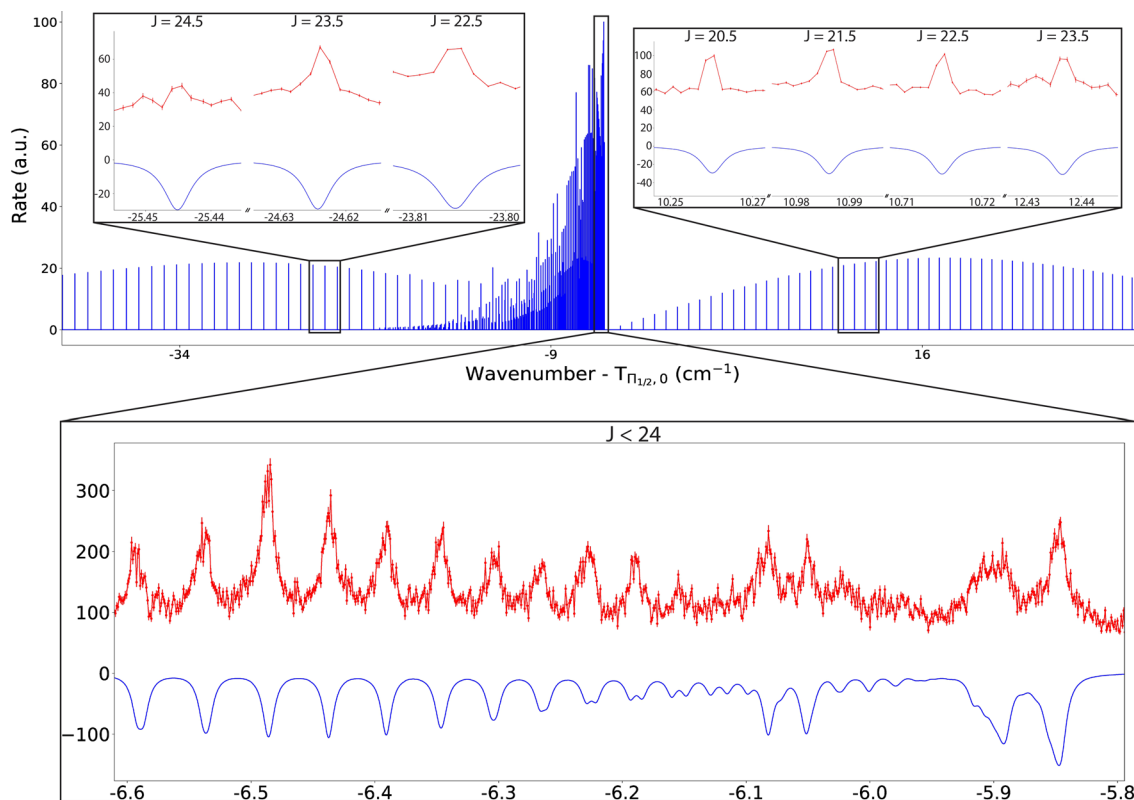
Extended Data Fig. 2 | Example of measured spectra for the $1' \leftarrow 1''$ transitions. In the centre, in blue, we present the simulated RaF spectrum for $J \leq 100$, over a range of ~ 70 cm^{-1} (J is the rotational quantum number of the rotational levels in the $X^2\Sigma^+$ electronic level). Figures in magnified views show measured spectra for different regions (note the broken x-axis present in some of the figures). The connected red dots show the experimental data, whereas the continuous blue line represents the best fit to the data. The errorbars indicate one standard deviation statistical uncertainty. For each spectrum we also show the covered range of J-values (see the main text and Methods for the details of the fit). The values on the x-axis correspond to the wavenumber of the first laser used in the excitation-ionization scheme, Doppler-corrected to the molecular rest frame and shifted by $T_{\Pi_{1/2,0}} = 13284.427$ cm^{-1}. On the y-axis we show the rate in arbitrary units (a.u.).

Extended Data Fig. 3 | Location of the bandheads in the $0' \leftarrow 0''$ rovibronic transitions. The bandhead locations are indicated with green arrows. The red dots represent the measured data while the blue line is the best fit to the data (see Methods for the details of the fit). The x-axis corresponds to the wavenumber of the first laser used in the excitation-ionization scheme, Doppler-corrected to the molecular rest frame and shifted by $T_{\Pi_{1/2,0}} = 13284.427\ \text{cm}^{-1}$. The y-axis shows the rate in arbitrary units (a.u.). The errorbars show one standard deviation statistical uncertainty.
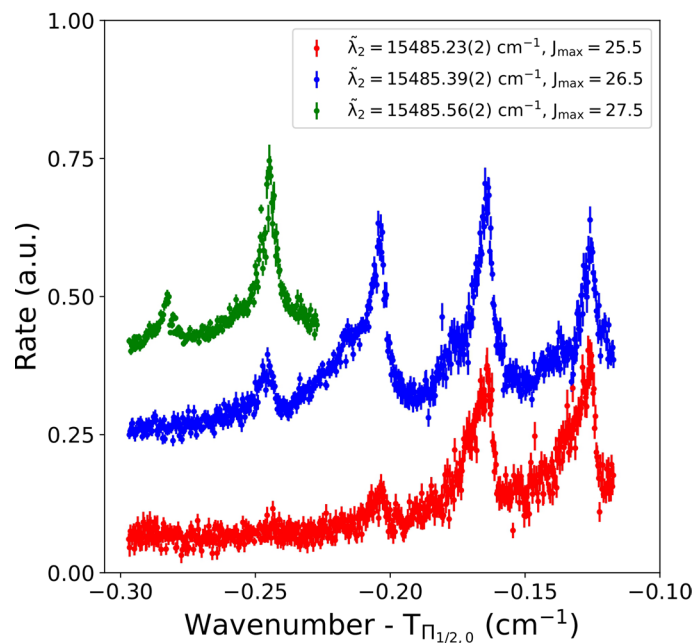
Extended Data Fig. 4 | Example of $0' \leftarrow 0''$ rovibronic spectra for different second-step laser wavenumbers. The red, blue and green dots correspond to separate scans of the first step laser, while the second-step laser wavenumber, Doppler-shifted to the molecular rest frame, was kept fixed at 15485.23(2) cm^{-1}, 15485.39(2) cm^{-1}, and 15485.56(2) cm^{-1}, respectively. Increasing the wavenumber of the second-step laser facilitated the observation of new transitions starting from levels with higher rotational quantum numbers, J, in the A$^2\Pi_{1/2} \leftarrow$ X$^2\Sigma^+$ spectrum (the new peaks appearing on the left). The maximum J-value of the shown spectra increases from $J_{max} = 25.5$ to $J_{max} = 27.5$. The x-axis corresponds to the wavenumber of the first laser used in the excitation-ionization scheme, Doppler-corrected to the molecular rest frame and shifted by $T_{\Pi_{1/2,0}} = 13284.427$ cm^{-1}. The y-axis shows the rate in arbitrary units (a.u.). The errorbars show one standard deviation statistical uncertainty.

Extended Data Table 1 | Vibrationally independent rotational constants of the $X^2\Sigma^+$ and $A^2\Pi_{1/2}$ electronic states

Parameter	This work
B_e''	0.19252(2)[4]
α_B''	0.00107(4)[6]
$10^7 \times D_e''$	1.50(17)[25]
$10^7 \times \alpha_D''$	0.20(31)[41]
γ_e	0.00587(5)[13]
α_γ	0.00004(6)[17]
B_e'	0.19154(2)[4]
α_B'	0.00105(4)[6]
$10^7 \times D_e'$	1.35(17)[25]
$10^7 \times \alpha_D'$	-0.10(31)[41]
p_e	-0.41118(7)[15]
α_p	-0.0009(1)[2]
$10^7 \times p_{D,e}$	0.7(10)[10]
$10^7 \times \alpha_{pD}$	-2.5(20)[16]

The first column shows the names of the parameters, while the second column shows their values in cm⁻¹. We show the 1σ statistical and systematic uncertainties in round and square brackets, respectively.